Influence of Solid-State Microstructure on the Electronic Performance of 5,11-Bis(triethylsilylethynyl) Anthradithiophene

15 AUTHORS, INCLUDING:

Xiaoran Li
Océ Technologies (a Canon Group Company)
15 PUBLICATIONS **155** CITATIONS

SEE PROFILE

Egon Pavlica
University of Nova Gorica
27 PUBLICATIONS **169** CITATIONS

SEE PROFILE

Ivan da Silva
Science and Technology Facilities Council
44 PUBLICATIONS **186** CITATIONS

SEE PROFILE

Charlotte Kjellander
TNO
12 PUBLICATIONS **265** CITATIONS

SEE PROFILE

Influence of Solid-State Microstructure on the Electronic Performance of 5,11-Bis(triethylsilylethynyl) Anthradithiophene

Liyang Yu,*[†] Xiaoran Li,*[#,§] Egon Pavlica,[‡] Felix P. V. Koch,[⊥] Giuseppe Portale,[‖] Iván da Silva,[∇,O] Marsha A. Loth,[¶] John E. Anthony,[¶] Paul Smith,[⊥,★] Gvido Bratina,[‡] B. K. Charlotte Kjellander,[§] Cornelis W. M. Bastiaansen,[#] Dirk J. Broer,[#] Gerwin H. Gelinck,[§] and Natalie Stingelin[†, ◆]

[†]Department of Materials and Centre for Plastic Electronics, Imperial College London, London, SW7 2AZ, United Kingdom,

[#]Department of Chemical Engineering and Chemistry, Technische Universiteit Eindhoven, Eindhoven, P.O. Box 513 5600 MB, The Netherlands,

[§]Holst Centre/TNO, High Tech Campus 31, Eindhoven, 5656 AE, The Netherlands,

[‡]Laboratory of Organic Matter Physics, University of Nova Gorica, Nova Gorica, SI-5000, Slovenia,

[⊥]Department of Materials, Eidgenössische Technische Hochschule (ETH) Zürich, Wolfgang-Pauli-Strasse 10, Zürich, 8093, Switzerland,

[‖]Netherlands Organization for Scientific Research, NOW, BM26B at the European Synchrotron Radiation Facility (ESRF), 6, rue Jules Horowitz, Grenoble, 38043, France,

[∇]SpLine Spanish CRG Beamline at the European Synchrotron Radiation Facility (ESRF), 6, rue Jules Horowitz, Grenoble, 38043, France,

[O]Instituto de Ciencia de Materiales de Madrid-ICMM/CSIC, Cantoblanco Madrid 28049, Spain,

[¶]Center for Applied Energy Research, University of Kentucky, Lexington, Kentucky 40511, United States ,

[★]Department of Physics and Centre for Plastic Electronics, Imperial College London, London, SW7 2AZ, United Kingdom,

[◆]FRIAS, School of Soft Matter Research, University of Freiburg, Freiburg, 79104, Germany

Ⓢ *Supporting Information*

ABSTRACT: The rich phase behavior of 5,11-bis-(triethylsilylethynyl) anthradithiophene (TES ADT) — one of the most promising, solution-processable small-molecular organic semiconductors — is analyzed, revealing the highest performing polymorph among four solid-state phases, opening pathways toward the reliable fabrication of high-performance bottom-gate/bottom-contact transistors.

KEYWORDS: *field-effect transistor, small molecule organic semiconductor, phase behavior, polymorphism, 5,11-bis(triethylsilylethynyl) anthradithiophene (TES ADT)*
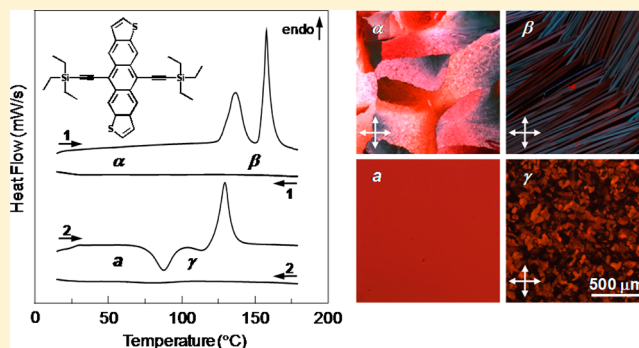
INTRODUCTION

Solution-processable organic π-conjugated small molecules have been demonstrated to show great potential as active elements in electronic devices such as organic field-effect transistors (OFETs),[1−3] organic solar cells,[4,5] and light-emitting diodes.[6,7] Thereby, 5,11-bis(triethyl silylethynyl) anthradithiophene (TES ADT) is one of the more promising materials for transistor applications because it can be readily synthesized at relatively large quantities,[8,9] and OFET devices of charge-carrier mobilities as high as 1.3 cm^2 V^{-1} s^{-1} and on/off ratios of more than 10^6 have been demonstrated using this small molecular compound.[8,10] However, until recently, the remarkable electronic performance of TES ADT has been challenging to reproduce in high yield, and the OFET mobility values reported in the literature for solution-processed structures cover 6 orders of magnitudes.[8−13] This discrepancy in device performance can at least partially be attributed to the fact that charge transport in small-molecule organic semiconductors is governed by the extent of intermolecular interactions, including the basic motifs the molecules arrange in such architectures,[8,14−16] which in

turn strongly depends on the deposition method and selected processing conditions. For TES ADT, for example, spin-coating yields predominantly amorphous thin films where charge transport is inevitably limited by the poor molecular order.[11] By contrast, solution casting (e.g. "drop casting") often results in highly crystalline structures − although they do not necessarily display a good device performance because the degree of crystallinity, crystalline perfection and orientation, grain size, and presence of grain boundaries as well as other features such as film roughness can strongly influence their OFET characteristics.[17−21]

Intriguingly, we recently found that casting TES ADT at 5 °C (i.e., well below this material's glass transition) allowed reliable fabrication of high-performance bottom-gate/bottom-contact transistors device performance.[10] For this purpose, close to 100 OFETs were tested, all displaying highly uniform device characteristics. While we tentatively attributed the beneficial influence of the use of a low deposition temperature to the fact that the solvent evaporation rate is reduced and hence, potentially, the solidification rate, the lack of even the most basic interrelationships between processing, structure, and device performance has stifled the design of processing procedures targeted for inducing, from the out-set and in a controlled manner, high-mobility structures and crystalline forms in a range of promising small-molecule semiconductors. As a matter of fact, to date, the development of procedures resulting in high-efficiency small-molecule devices has notoriously relied on intricate trial-and-error procedures to gradually optimize device performance.

We here set out to elucidate how processing and thermal post treatment procedures can affect the thin-film structure of small-molecule semiconductors and, as a consequence, their electronic properties. We focused on TES ADT and assessed this material's thermal behavior, accessible solid-state phases, and charge-transport properties deduced from OFET device characteristics as well as lateral time-of-flight (L-ToF) photoconductivity measurements of these materials. This allowed us to identify the best performing TES ADT polymorph among three crystalline phases (and one amorphous one) therewith opening pathways which should allow identification of processing protocols that exclusively induce this specific polymorph for reliable fabrication of high-performance bottom-gate/bottom-contact transistors in addition to the low-temperature casting reported previously.[10]

■ EXPERIMENTAL SECTION

Materials. 5,11-Bis(triethyl silylethynyl) anthradithiophene (TES ADT) was synthesized according to the literature.[8]

Thin Film Preparation. Thin films for structural analysis as well as electronic characterizations were fabricated by dissolving TES ADT in chloroform (4 wt %), followed by solution (drop-) casting onto the corresponding substrate at 5 °C in ambient conditions.

Thermal Analysis. Differential scanning calorimetry (DSC) measurements were conducted under N_2 atmosphere at a scan rate of 10 °C min^{-1} with a Mettler Toledo STARe system DSC 1. Standard Mettler aluminum crucibles were used. The sample weight was ∼5 mg.

Optical Microscopy. Optical microscopy was carried out with an Olympus BX51 polarizing microscope equipped with a Q-imaging Go-3 camera and a Mettler Toledo FP82HT hot-stage.

X-ray Diffraction. Variable temperature wide-angle X-ray scattering (WAXS) and powder diffraction measurements were performed at BM26B-DUBBLE Dutch-Belgian beamline of the European Synchrotron Radiation Facility (ESRF)[25] equipped with a Linkam THMS600 temperature-controlled stage. The samples were in powder form obtained from the as-cast TES ADT films. The temperature-controlled

stage was programmed according to the DSC results. Powder diffraction measurements were performed also on thin film samples, which had been powdered and then placed inside 0.5-mm-diameter glass capillaries and rotated during exposure, using a large 1043 × 981 pixels Pilatus1M area detector, positioned orthogonally to the incoming beam direction. The pixel size was 172 × 172 μm^2 and the used X-ray wavelength was 1.033 Å. Calibration of wavelength and sample−detector distance was achieved using a NIST standard LaB6 sample, while azimuthal integration of recorded images was performed with XOP software,[26] and Rietveld refinement of the thin film diffraction data for TES ADT α-phase was carried out using FULLPROF software.[27]

Density Measurements. Density measurements were conducted using a salt-water solution column with a continuous density gradient and floats with standard densities inside. The standard deviation is given by the distribution of materials in the column as observed by eye.

Electronic Characterization. Thin films of the various TES ADT polymorphs for assessment of their electronic properties were obtained by first casting thin films on pretreated transistor or L-ToF substrates (see below) and annealing them in the different phase-regions identified in thermal analysis. For transistor fabrication, we employed Si (n^{++})/SiO$_2$ substrates with photolithographically prepatterned Au as source/drain electrodes in a bottom-gate/bottom-contact geometry. The Au electrodes were treated with pentafluorobenzenethiol (PFBT),[8] while for the SiO$_2$ trichlorophenylsilane (TCPS)[28,29] was used, to reduce the contact resistance and improve the dielectric interface, respectively. Transistor device characteristics were measured at room temperature in inert atmosphere using an Agilent 4155C semiconductor parameter analyzer. For L-ToF measurements, prior to TES ADT deposition, two parallel aluminum electrodes 160 μm apart from each other were deposited onto glass substrates. Using aluminum as the electrode material the dark current was minimized. Consequently the dielectric relaxation time was extended over the transit time. The TES ADT was subsequently solution-cast on these substrates and annealed into different solid-state phases, as described above. For the L-ToF measurements, the laser pulse duration was approximately 3 ns. The laser beam was focused to a 10 μm width line with a cylindrical lens near the source electrode. Voltages were generated by a CAEN N1470 power supply, and the current of the drain electrode was measured with a 2.5 GHz Lecroy WavePro 725Zi oscilloscope in ambient atmosphere. An Ekspla NT342 tunable wavelength laser (pulsed) was employed for the measurements. The energy of laser pulse was adjusted in order to obtain linear dependence between photocurrent magnitude and pulse intensity since the former is proportional to the product of the amount of the photogenerated carriers and their mobility. Thereby we approximated the amount of photogenerated charges to be constant. In accordance with our measurements, the magnitude of photocurrent indeed increased with mobility. The Scher-Montroll approximation[30] was used to fit the photocurrents to identify the transit times t_{tr} according to

$$I(t) = \begin{cases} k \cdot t^{-\alpha_1}, & t < t_{tr} \\ k \cdot t_{tr}^{(\alpha_2-\alpha_1)} \cdot t^{-\alpha_2}, & t \geq t_{tr} \end{cases}$$

where k is a proportionality constant, and α_1 and α_2 are dispersive parameters. In $\log(I) - \log(t)$ plots this resulted in

$$\log(I) = \begin{cases} \log(k) - \alpha_1 \cdot \log(t), & t < t_{tr} \\ \log(k) + (\alpha_2 - \alpha_1) \cdot \log(t_{tr}) - \alpha_2 \cdot \log(t), & t \geq t_{tr} \end{cases}$$

The coefficients α_1 and α_2 for different polymorphs are given in Table 1.

Note that in order to calculate the time-of-flight mobility, we assumed that the electric field between coplanar electrodes is constant. We acknowledge that this can represent a notable correction to the mobility estimation, which we believe was compensated by the uncertain readout of the transit time from the photocurrent change of slope in double logarithmic plot. Readout uncertainty was caused due

Table 1. Parameters of the Scher-Montroll Photocurrent Approximation,[30] Which Was Used To Fit the L-ToF Phototransients Presented in Figure 3[a]

phase	k [As]	α_1	α_2	t_{tr} [s]
alpha	0.82	0.23	0.56	1.12×10^{-5}
beta	4.37×10^{-4}	0.527	0.821	3.78×10^{-4}
gamma	0.0106	0.289	0.572	3.22×10^{-5}
amorphous	8.3×10^{-5}	0.334	0.931	0.013

[a]Parameters were obtained by the least-chi square fit.

to the relatively broad region where the photocurrent changes slopes. We attribute this to undesirable grain boundary effects. We like to emphasize, though, that transient times scaled with bias voltage as required, with the most significant fluctuations found for the β-phase due to a high noise to signal ratio.

■ **RESULTS AND DISCUSSION**

In the first set of experiments, we assessed the rich thermal behavior of TES ADT using DSC and variable-temperature polarized optical microscopy (POM). For samples of thin films produced by casting solutions of 4 wt % TES ADT in chloroform at 5 °C, we observe two endothermic transitions around 135 and 155 °C during heating from room temperature to 175 °C (Figure 1a), in agreement with the data published by Chung et al.[22] In optical microscopy, a drastic change in microstructure is found at the first transition (135 °C): from a highly birefringent, continuous terrace-like architecture with domain sizes of 500 μm or more (hereafter referred to as α-phase), to well-defined, single-crystal-like needles of 20 μm width and a few millimeters in length (β-phase; Figure 1b/top panels). At temperatures above 155 °C, all birefringence was lost indicating the melting of the material.

During cooling from the melt at a rate of 10 °C min^{-1}, no crystallization endotherm was recorded in DSC (Figure 1a). In agreement, in optical microscopy, thin films produced from the melt using identical cooling rates as in the thermal analysis were found to be amorphous (denoted: a-phase), as is evident from their featureless appearance in unpolarized light (Figure 1b, left bottom panel) and the lack of birefringence between crossed polarizes (not shown). Interestingly, upon heating this glassy structure, the phase behavior differed from the one observed for as-cast films. At ∼27 °C, a glass transition temperature (T_g) of this vitreous TES ADT was observed. The material then recrystallized at temperatures above 80 °C, resulting in birefringent structures comprising domains of around 20 μm in size (γ-phase; Figure 1b, right bottom panel). This γ-phase melted at 130 °C as deduced from the endotherm observed at this temperature in thermal analysis (Figure 1a) and the disappearance of all birefringence detected in POM.

It is evident from these initial experiments that TES ADT shows polymorphism with at least four solid-state phases (three crystalline ones i.e. α, β, γ and one amorphous structure, i.e. a), with their formation depending on processing history and thermal (post)treatment. Importantly, our data also imply that the low-temperature-cast phase which previously showed very promising and highly reproducible device characteristics[10] is metastable; meaning that once it is heated and the β- or γ-phase is formed, it cannot be induced any longer.

This latter observation is confirmed by variable-temperature wide-angle X-ray scattering (WAXS). The as-cast film (α-phase) featured sharp and well-defined reflections (Figure 1c). Upon heating such films, at ∼140 °C, distinctly different
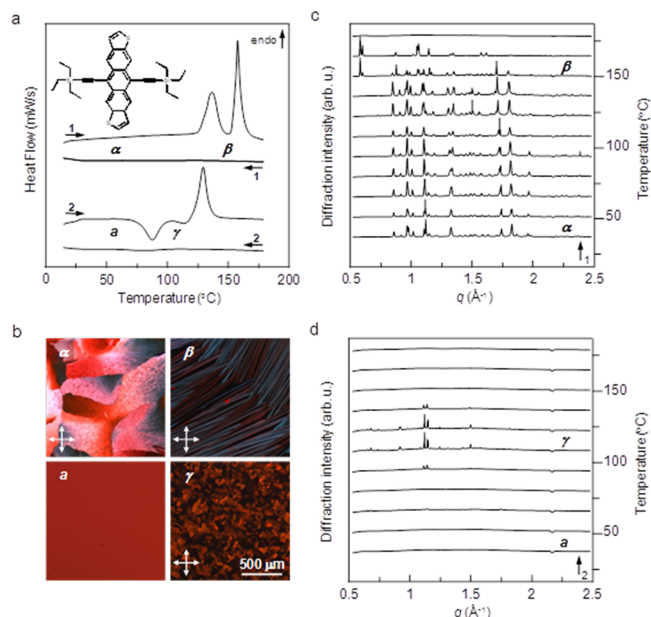

Figure 1. a) Differential scanning calorimetry (DSC) heating and cooling thermograms of TES ADT powder obtained from films cast from solutions of 4 wt % TES ADT in chloroform at 5 °C and then heat-treated. The chemical structure of TES ADT is shown in the inset. b) Corresponding optical micrographs of films of as-cast TES ADT at room temperature (α-phase; top left); the β-phase, as observed at 150 °C (top right); amorphous TES ADT (a-phase) obtained when cooling from the isotropic melt (bottom right); and the γ-phase (at 100 °C) that develops during heating of the a-phase (bottom left). [Note, the micrographs of the α-, β-, and γ-phase were taken between crossed polarisers]. c, d) Variable-temperature wide-angle X-ray scattering (WAXS) patterns of solution-cast TES ADT films that were subsequently heated, molten, and recrystallized from the solid state. c) First heating cycle (1): initially the α-polymorph is present; at 150 °C the β-phase is found to form. d) Second heating cycle (2): The initially amorphous structure (a-phase) recrystallizes, and the γ-polymorph is detected at temperatures above 80 °C. Melting of this phase (γ) is deduced from the disappearance of all reflections (occurring at 130 °C).

diffraction patterns emerged with a prominent reflection at $q \sim$ 0.6 Å^{-1}, indicating the formation of the β-phase. All reflections disappeared at temperatures above 160 °C in agreement with the DSC endotherm at 155 °C being the melting transition. No detectable reflections were recorded upon cooling the film, again in accord with our thermal analysis and optical microscopy data. The γ-phase can be seen to develop at ∼80 °C (Figure 1d).

Clearly, the rich phase behavior of TES ADT, and in particular the presence of metastable phases such as the α-polymorph, may explain the spread in device performance that has been observed in the literature for this specific small-molecule semiconductor because slight variations in processing conditions can introduce different crystal forms. In order to gain more insight in the latter and investigate how the solid-state properties of the identified TES ADT phases differ, we produced films comprised of, respectively, the α-, β-, γ-, or a-phase. Thereby, films of the β- and γ-phase were prepared by first inducing the respective polymorph at the relevant temperature and then quenching the structure directly to room temperature, while α- and a-structures were realized by, respectively, low-temperature casting as described in ref 10 (α-phase) or rapid cooling from the melt (a-phase). WAXS data
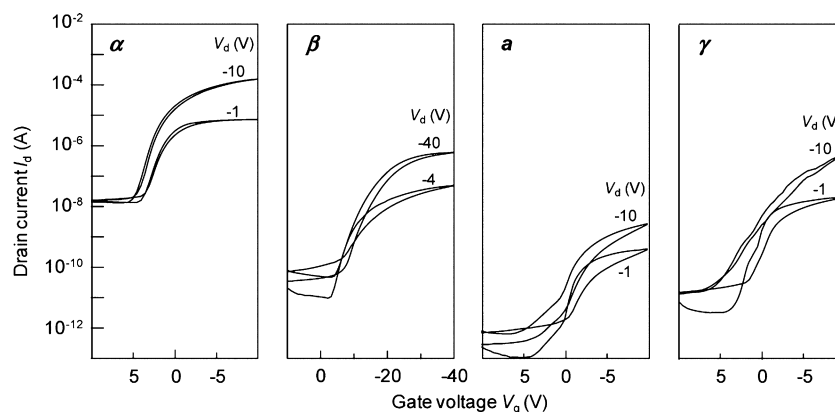
Figure 2. Representative transfer characteristics of transistors prepared with the various TES ADT structures, i.e. the crystalline α-, β-, and γ-polymorph and the amorphous a-phase, realized by either solution-casting at 5 °C (α-phase), or first inducing the respective polymorph at the relevant temperature and then quenching the structure directly to room temperature (β- and γ-phase). Amorphous structures were fabricated by rapid cooling from the melt (a-phase). The devices were measured at room temperature since in situ charge-transport measurements inOFET structures can be flawed as changes in temperature can strongly affect device mobility also for materials that do not have phase transitions in the regime tested. This is particularly true for materials where charge transport depends on charge hopping. Note that for the β-phase, V_g was swept from +10 V to −40 V, using a $V_d = −4$ V and −40 V as the devices were not operational at lower voltages.

taken from those samples at 25 °C confirmed that these procedures originated in films of the different TES ADT structures (see Supporting Information Figure S1). Also, distinctly different UV−vis spectra were recorded at room temperature for thin-film architectures produced in this manner (Supporting Information Figure S2).

First, we determined the density (ρ) of the different TES ADT phases to obtain an indication of the difference in molecular packing between them. We find that the α- and β-phase are of very comparable densities: respectively, $\rho(\alpha) = 1.146 \pm 0.004$ g cm^{-3} and $\rho(\beta) = 1.144 \pm 0.002$ g cm^{-3}. The γ-phase is significantly less dense than the other two crystalline polymorphs ($\rho(\gamma) = 1.128 \pm 0.006$ g cm^{-3}), although the amorphous TES ADT featured the lowest density ($\rho(a) = 1.115 \pm 0.004$ g cm^{-3}).

Device performance (at room temperature) of the identified TES ADT phases differed significantly. Representative transfer characteristics for the α-, β-, γ-, and a-phase are presented in Figure 2. (Corresponding output characteristics and a square root plot of source-drain current are shown in the Supporting Information Figure S3). The average saturation mobilities deduced from these characteristics are 0.4 cm^2 V^{-1} s^{-1} (α), 1×10^{-3} cm^2 V^{-1} s^{-1} (β), 5×10^{-3} cm^2 V^{-1} s^{-1} (γ), and 5×10^{-6} cm^2 V^{-1} s^{-1} (a). The α-phase, which is the densest structure, yielded the best OFET characteristics in terms of mobility, on-current, subthreshold slope, and absence of hysteresis between backward and forward scans. However, the β-phase, which is of almost the same density, displayed considerably inferior OFET characteristics and required analysis at a higher gate (and drain) bias to produce working devices. This is possibly due to the pronounced surface roughness (which is known to limit OFET performance) of films prepared from this polymorph compared to structures prepared with the α-phase (see Supporting Information Figure S4). The γ-phase, which is of lower density than both the α- and β-TES ADT, displayed higher charge-carrier mobilities compared to the latter polymorph, despite the fact that it features a similar roughness as β. We like to note, though, that devices made of the γ-phase were limited by a relatively pronounced hysteresis. Expectedly, the poorest device performance was found for the amorphous TES ADT structures.

In order to exclude the possibility of the observed difference in OFET performance among the various TES ADT phases being a result of parasitic effects, such as poor dielectric−semiconductor interfaces and/or charge-injection limitations, rather than the molecular packing or surface roughness, we also performed L-ToF photoconductivity measurements (for details see: Experimental Section), where the influence of device geometry and contact resistance can be eliminated and native bulk charge-carrier mobility is measured in-plane of the thin films allowing direct comparison with the OFET data. Typical L-ToF phototransients are displayed in Figure 3. From the transit time t_{tr}, i.e. the time it takes the photogenerated charges to reach the opposite electrode, deduced from the change of slope of the double logarithmic plots of current vs time (indicated with arrows in Figure 3), we can calculate the
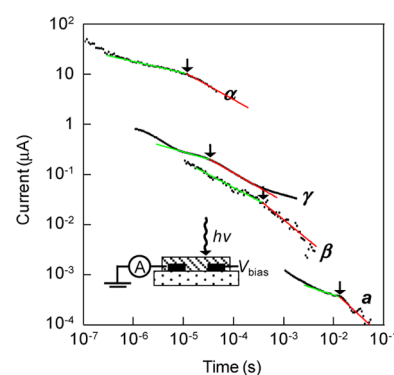

Figure 3. Lateral time-of-flight (L-ToF) transient photocurrents measured on thin films of TES ADT's various phases ($V = 800$ V). The photocurrents are displayed with respect to each other for the purpose of clarity. The position of the transit times t_{tr} for the respective phases, obtained from corresponding fits (red and green lines) using the Scher-Montroll approximation,[30] are indicated with arrows. A schematic view of the lateral time-of-flight transient photoconductivity measurement setup comprised of coplanar electrodes is shown in the inset. The laser pulse illumination is confined to the biased electrode, and charge transport is measured in-plane as in transistor devices.

charge-carrier mobilities (μ_{TOF}) for the different TES ADT architectures from $\mu_{TOF} = L^2 t_{tr}^{-1} V_{bias}^{-1}$.

Again, the β-phase displayed significantly inferior charge-carrier mobilities compared to the α-phase ($\mu_{TOF}(\beta) \approx 2 - 8.5 \times 10^{-4}$ cm^2 V^{-1} s^{-1} vs $\mu_{TOF}(\alpha) \approx 0.046$ cm^2 V^{-1} s^{-1} at 800 V), indicating that charge transport in this TES ADT structure was not limited in transistors due to e.g. a significant difference in dielectric interface quality. Note also that charge transport in the needle-shaped structures of the TES ADT β-phase was not strongly dependent on the direction in which charge transport was assessed: parallel and perpendicular to the needles we deduced L-ToF mobilities of, respectively, 8.5×10^{-4} cm^2 V^{-1} s^{-1} and 2×10^{-4} cm^2 V^{-1} s^{-1} (channel length = 160 μm; V = 800 V). The amorphous phase displayed minimum values of μ_{TOF} of 2.5×10^{-5} cm^2 V^{-1} s^{-1}. The electronic performance of such amorphous films significantly improved, however, upon recrystallization to the γ-phase, with $\mu_{TOF}(\gamma)$ reaching 9.9×10^{-3} cm^2 V^{-1} s^{-1} (at 800 V).

Clearly, the metastable α-polymorph, which we have recently discovered when low-temperature casting TES ADT solutions, is the polymorph of the best charge transport properties among all the phases we have identified here. This illustrates the importance of identifying the solid-state phases a material can exhibit because their attributes may be drastically different. The latter is especially true for small-molecule and oligomeric semiconductors which are prone to polymorphism. The question that remains is why α-phase of TES ADT is so favorable for charge transport. For this purpose, we conducted X-ray powder diffraction on solution-cast thin-film architectures of the α-phase, which had been powdered and placed in glass capillaries that rotated during the measurements (see the Materials and Methods section and Supporting Information Figure S5 for details).

We find that the structure of the thin-film α-phase is very comparable to the 2D π-stacking arrangement reported for TES ADT single crystals;[8] which possibly explain the excellent electronic performance of this polymorph. The average distance between π-faces is 3.38 Å (3.26 Å for the single crystal structure), and the π-overlap slippage is ~1.73 Å and ~3.08 Å (1.84 and 3.23 Å for the single crystal structure).[8] The unit cell of the thin film structure seems somewhat distorted (or "strained") compared to the single crystal, which has recently been shown to drastically influence the electronic performance of small molecule, organic semiconductors: the a- and b-axis of the unit cell are larger in the thin film ($a = 6.8739$ Å, $b = 7.4075$ Å, compared to $a = 6.7318$ Å, $b = 7.2511$ Å in single-crystalline TES ADT), while the c-axis dimension remains almost unchanged.[23] However, the α and β angles are smaller in the thin films (see for a comparison of the two crystal structures Supporting Information Figure S6). Furthermore, grazing-incidence diffraction analysis of thin α-phase films (not shown here) indicates that in such α-TES ADT films, the (00l) planes are oriented perpendicular to the substrate. This has been shown to often lead to favorable charge transport pathways.[24] Thereby the tilt angle of the aromatic plane with respect to the substrate is ~71.59°.

CONCLUSION

In summary, of all the various solid state phases that we could identify for TES ADT, the crystalline α-form displays the best device performance. Our X-ray and microscopy data suggest that this polymorph corresponds to the high mobility structure that can also be obtained through solvent vapor annealing. This specific polymorph possibly shows the highest charge-carrier motilities because it forms relatively smooth films and is of a very comparable crystalline structure as TES ADT single crystals but slightly strained and with the (00l) planes oriented perpendicular to the substrate. This indicates that also for other small-molecule semiconductors single-crystal structure data can guide identification of high-performance thin-film architectures. We currently identify the precise structures of the β- and γ-phase. So far, we understand that the β-phase is triclinic, while the γ-phase features a monoclinic unit cell. Our data clearly show that selection of processing conditions is critical; slight variations and ill-selected annealing procedures will induce phases of significantly inferior device performance than the single-crystal-like structure. This may explain the broad range of charge-carrier mobility values that have been reported in the literature for TES ADT and similar small-molecule semi-conductors; also, it raises the question if polymer binders may have a strong influence on the phase behavior of TES ADT, possibly inducing the required polymorph. Without doubt, more detailed information on the other TES ADT phases will be required to obtain a full understanding of relevant structure/ processing/property/performance- interrelationships from the molecular to the macroscale of this interesting and promising organic semiconductor, and especially why low-temperature casting induces a polymorph of very similar structure as single crystals. Nonetheless, identification of the optimally performing phase is a first step toward such an understanding, and it will permit the development of processing protocols that allow deposition of TES ADT into the phase showing the best device performance, preventing formation of the low(er) mobility structures such as the β-, γ-, or a-phase, over large areas.

ASSOCIATED CONTENT

Ⓢ Supporting Information

X-ray diffraction data, additional OFET characteristics, surface profilometry results for α-, β-, γ- and amorphous phases, final Rietveld refinement X-ray diffraction plots for TES ADT's α-phase and a comparison of the unit cell structure of this thin film structure and TES ADT single crystals. This material is available free of charge via the Internet at http://pubs.acs.org.

AUTHOR INFORMATION

Corresponding Author

*E-mail: liyang.yu@kaust.edu.sa.

Notes

The authors declare no competing financial interest.

■ REFERENCES

(1) Dodabalapur, A. *Mater. Today* **2006**, *9*, 24.

(2) Gelinck, G.; Heremans, P.; Nomoto, K.; Anthopoulos, T. D. *Adv. Mater.* **2010**, *22*, 3778.

(3) Zhang, L.; Di, C.; Yu, G.; Liu, Y. *J. Mater. Chem.* **2010**, *20*, 7059.

(4) Mishra, A.; Bäuerle, P. *Angew. Chem.* **2012**, *51*, 2020.

(5) Beaujuge, P. M.; Fréchet, J. M. J. *J. Am. Chem. Soc.* **2011**, *133*, 20009.

(6) Duan, L.; Hou, L.; Lee, T. W.; Qiao, J.; Zhang, D.; Dong, G.; Wang, L.; Qiu, Y. *J. Mater. Chem.* **2010**, *20*, 6392.

(7) Cai, M.; Xiao, T.; Hellerich, E.; Chen, Y.; Shinar, R.; Shinar, J. *Adv. Mater.* **2011**, *23*, 3590.

(8) Payne, M. M.; Parkin, S. R.; Anthony, J. E.; Kuo, C. C.; Jackson, T. N. *J. Am. Chem. Soc.* **2005**, *127*, 4986.

(9) Anthony, J. E. *Chem. Rev.* **2006**, *106*, 5028.

(10) Yu, L.; Li, X.; Pavlica, E.; Loth, M. A.; Anthony, J. E.; Bratina, G.; Kjellander, C.; Gelinck, G.; Stingelin, N. *Appl. Phys. Lett.* **2011**, *99*, 263304.

(11) Dickey, K. C.; Anthony, J. E.; Loo, Y. L. *Adv. Mater.* **2006**, *18*, 1721.

(12) Lee, W. H.; Lim, J. A.; Kim, D. H.; Cho, J. H.; Jang, Y.; Kim, Y. H.; Han, J. I.; Cho, K. *Adv. Funct. Mater.* **2008**, *18*, 560.

(13) Lee, W. H.; Kim, D. H.; Cho, J. H.; Jang, Y.; Lim, J. A.; Kwak, D.; Cho, K. *Appl. Phys. Lett.* **2007**, *91*, 092105.

(14) Anthony, J. E. *Angew. Chem.* **2008**, *47*, 452.

(15) Karl, N. *Synth. Met.* **2003**, *133−134*, 649.

(16) Shtein, M.; Mapel, J.; Benziger, J. B.; Forrest, S. R. *Appl. Phys. Lett.* **2002**, *81*, 268.

(17) Gundlach, D. J.; Royer, J. E.; Park, S. K.; Subramanian, S.; Jurchescu, O. D.; Hamadani, B. H.; Moad, A. J.; Kline, R. J.; Teague, L. C.; Kirillov, O.; Richter, C. A.; Kushmerick, J. G.; Richter, L. J.; Parkin, S. R.; Jackson, T. N.; Anthony, J. E. *Nat. Mater.* **2008**, *7*, 216.

(18) Sele, C. W.; Kjellander, B. K. C.; Niesen, B.; Thornton, M. J.; van der Putten, J. B. P. H.; Myny, K.; Wondergem, H. J.; Moser, A.; Resel, R.; van Breemen, A. J. J. M.; van Aerle, N.; Heremans, P.; Anthony, J. E.; Gelinck, G. H. *Adv. Mater.* **2009**, *21*, 4926.

(19) Rivnay, J.; Jimison, L. H.; Northrup, J. E.; Toney, M. F.; Noriega, R.; Lu, S.; Marks, T. J.; Facchetti, A.; Salleo, A. *Nat. Mater.* **2009**, *8*, 952.

(20) Salleo, A.; Kline, R. J.; DeLongchamp, D. M.; Chabinyc, M. L. *Adv. Mater.* **2010**, *22*, 3812.

(21) McCulloch, I.; Heeney, M.; Chabinyc, M. L.; DeLongchamp, D.; Kline, R. J.; Cölle, M.; Duffy, W.; Fischer, D.; Gundlach, D.; Hamadani, B.; Hamilton, R.; Richter, L.; Salleo, A.; Shkunov, M.; Sparrowe, D.; Tierney, S.; Zhang, W. *Adv. Mater.* **2009**, *21*, 1091.

(22) Chung, Y. S.; Shin, N.; Kang, J.; Jo, Y.; Prabhu, V. M.; Satija, S. K.; Kline, R. J.; DeLongchamp, D. M.; Toney, M. F.; Loth, M. A.; Purushothaman, B.; Anthony, J. E.; Yoon, D. Y. *J. Am. Chem. Soc.* **2011**, *133*, 412.

(23) Giri, G.; Verploegen, E.; Mannsfeld, S. C. B.; Atahan-Evrenk, S.; Kim, D. H.; Lee, S. Y.; Becerril, H. A.; Aspuru-Guzik, A.; Toney, M. F.; Bao, Z. *Nature* **2011**, *480*, 504.

(24) Stingelin-Stutzmann, N.; Smits, E.; Wondergem, H.; Tanase, C.; Blom, P.; Smith, P.; de Leeuw, D. *Nat. Mater.* **2005**, *4*, 601.

(25) Nikitenko, S.; Beale, A. M.; Van Der Eerden, A. M. J.; Jacques, S. D. M.; Leynaud, O.; O'Brien, M. G.; Detollenaere, D.; Kaptein, R.; Weckhuysen, B. M.; Bras, W. *J. Synchrotron Radiat.* **2008**, *15*, 632.

(26) Sánchez del Río, M. Synchrotron Data Analysis Using XOP, in Synchrotron Radiation in Mineralogy, Seminarios De La Sociedad Española De Mineralogía, 2009; Vol. *6*, pp 109−141.

(27) Rodriguez-Carvajal, J. *Commission on Powder Diffraction (IUCr) Newsletter* **2001**, *26*, 12.

(28) Li, X.; Kjellander, B. K. C.; Anthony, J. E.; Bastiaansen, C. W. M.; Broer, D. J.; Gelinck, G. H. *Adv. Funct. Mater.* **2009**, *19*, 3610.

(29) Kumaki, D.; Yahiro, M.; Inoue, Y.; Tokito, S. *Appl. Phys. Lett.* **2007**, *90*, 133511.

(30) Scher, H.; Montroll, E. W. *Phys. Rev. B* **1975**, *12*, 2455.